Thermalization of dense hadronic matter in Au + Au collisions at energies available at the Facility for Antiproton and Ion Research

Somnath De,[1] Sudipan De,[2] and Subhasis Chattopadhyay[3]
[1]*Institute of Physics, Bhubaneswar, Odisha 751005, India*
[2]*Universidade de São Paulo, 05508-090 São Paulo, Brazil*
[3]*Variable Energy Cyclotron Centre, 1/AF, Bidhan Nagar, Kolkata, 700064, India*
(Received 6 October 2015; revised manuscript received 15 August 2016; published 7 November 2016)

The conditions of local thermodynamic equilibrium of baryons (nonstrange, strange) and mesons (strange) are presented for central Au + Au collisions at Facility for Antiproton and Ion Research (FAIR) energies using the microscopic transport model UrQMD. The net particle density, longitudinal-to-transverse pressure anisotropy, and inverse slope parameters of the energy spectra of nonstrange and strange hadrons are calculated inside a cell in the central region within rapidity window $|y| < 1.0$ at different time steps after the collisions. We observed that the strangeness content is dominated by baryons at all energies; however, contributions from mesons become significant at higher energies. The time scale obtained from local pressure (momentum) isotropization and thermalization of energy spectra are nearly equal and found to decrease with increase in laboratory energy. The equilibrium thermodynamic properties of the system are obtained with a statistical thermal model. The time evolution of the entropy densities at FAIR energies are found to be very similar to the ideal hydrodynamic behavior at top Relativistic Heavy Ion Collider (RHIC) energy.

DOI: 10.1103/PhysRevC.94.054901

I. INTRODUCTION

The motivation of the relativistic heavy ion collider experiments is to explore the properties of strongly interacting matter (partonic or hadronic) at the finite temperature and/or density. The current heavy ion research facilities, e.g., Relativistic Heavy Ion Collider (RHIC) and Large Hadron Collider (LHC), are focused on unveiling the properties of deconfined quark-gluon matter created at extreme temperatures and almost vanishing net baryon density [1,2]. At this regime the lattice quantum chromodynamics (lQCD) simulations have reported a crossover from hadronic to partonic phases and the existence of a critical point where the first-order phase transition line terminates [3]. Thus RHIC has initiated the beam energy scan program to find the location of a critical point in the QCD phase diagram [temperature (T)–baryochemical potential (μ_B) plane] [4].

In contrarst to the above experiments, the future Compressed Baryonic Matter (CBM) experiment at the FAIR/GSI Helmholtz Centre for Heavy Ion Research (GSI Helmholtzzentrum für Schwerionenforschung) laboratory is aimed to explore another facet of the QCD phase diagram, at high baryon density (∼7 to 8 times ground-state nuclear matter density) and moderate temperature [5,6]. The experiment would be playing a very significant role in the scientific quest of understanding the behavior of QCD at high density regime. The facility is being designed to collide various species of heavy ions at fixed target mode with anticipated beam energies of 5–45 GeV/nucleon. The diagnostic probes of the matter created in the collisions include (i) short-lived vector mesons (ρ, ω) decaying to dilepton pairs, (ii) production of multistrange hyperons (Ξ, Ω), (iii) dissociation of charmonium (J/Ψ) and charmed hadron (D, Λ_c) states, etc. The existence of a first-order phase transition from hadronic to partonic matter and restoration of chiral symmetry at the large μ_B is expected to be found from the FAIR energy scan program [7]. Earlier experiments such as Relativistic Heavy Ion Collider (RHIC)-Alternating Gradient Synchrotron (AGS) and Conseil Européen pour la Recherche Nucléaire (European Council for Nuclear Research) (CERN)-Super Proton Synchrotron (SPS) were aimed to explore the above features through the measurement of bulk observables like flow and momentum spectra of hadrons. However, their efforts were constrained due to limited beam luminosity. In recent years a similar research program (NICA) at JINR-Dubna has been proposed to explore phases of nuclear matter at high baryon density [8]. But the CBM experiment would be more efficient for the detection of bulk and rare probes, with the availability of high-intensity ion beams [9].

In order to compute the dynamic evolution of the matter created in such collisions, we need macroscopic and microscopic models. The macroscopic models like hydrodynamics rely upon the assumption of local thermal equilibrium of the created matter on a certain time scale. The actual thermalization criterion has seldom been tested. There are a few works that have addressed the issue at higher collision energies in the framework of perturbative QCD [10] or color-glass condensate theory [11]. On the other hand, microscopic Monte Carlo models like Ultra relativistic Quantum Molecular Dynamics (UrQMD) [12], Hadron String Dynamics (HSD) [13], and A Multi Phase Transport model (AMPT) [14] work on the postulated interaction among the constituents (parton, hadron, or string) and do not require any assumption of local thermal equilibrium. Therefore, it is very important to test whether the dense baryonic matter created in these collisions achieves a local thermal equilibrium or not. In particular, we have investigated the time scale of local thermal equilibration of nonstrange and strange baryons in an elementary volume in phase space from the time evolution of longitudinal-to-transverse pressure anisotropy and slope of the energy spectrum. For this purpose, we have employed the microscopic, N-body transport

model called ultrarelativistic quantum molecular dynamics (UrQMD). A comparison between the model and the data for central Pb+Pb collisions at different energies at CERN-SPS can be found in Ref. [15]. We considered the most central collisions of gold (Au) nuclei at four beam energies associated with the CBM experiment. The incident beam energy has obvious implications on the time scale of equilibration, which can be found in the subsequent section.

The organization of the paper is the following: In the next section, we briefly review the microscopic transport model UrQMD and then discuss the methodology of our analysis. In Sec. III, we show the results for the time evolution of density, ratio of longitudinal-to-transverse pressure, and inverse slope parameter of the energy spectra for nonstrange baryons, strange baryons, and strange mesons. In Sec. IV, we utilize the statistical thermal model to extract the postequilibrium thermodynamic parameters (e.g., temperature, chemical potentials) and calculated the entropy density of the system. Finally we summarize the findings in Sec. V.

II. METHODOLOGY OF THE ANALYSIS

The model UrQMD has been extensively used in recent years for describing heavy ion collisions of center-of-mass energy ranging from a few GeV/ nucleon to a few TeV/ nucleon [12]. We used the UrQMD version 3.3p2 in default cascade mode without invoking any hydrodynamic evolution for the initial state. It includes 55 baryon species (up to mass 2.25 GeV) and 32 meson species (up to mass 1.9 GeV) and their corresponding antiparticles and isospin-projected states. Particle production in UrQMD occurs through inelastic collisions, decay of mesons, baryon resonances, and string fragmentation. At low energies ($E_{\rm lab} < 4$ GeV) hadronic interactions are based on two- or three-body potential. However, at high energies, hadron-hadron collisions are performed stochastically in the spirit of the cascade model [16]. The total (elastic and inelastic) cross sections of baryons and mesons are generally fitted to experimental proton-proton or proton-pion scattering data. For the resonant baryon-meson or hyperon-baryon scattering where no experimental data are available, the principle of detail balance or the additive quark model have been used. The resonance scattering dominates the total cross section at low beam momenta (up to $p_{\rm lab} \sim 2$ GeV); however, toward higher beam momenta, string excitation has the largest contribution. The inelastic collisions and decays are responsible for changing the particle abundances of the system while the elastic collisions modify the momentum distribution of hadrons.

We have considered central collisions (impact parameter $b = 2$ fm) of Au nuclei at the laboratory energies ($E_{\rm lab}$) 10A, 20A, 30A, and 40A GeV. For each energy we ran the simulation at different time steps ranging from 1 to 15 fm/c; 6×10^4 events have been analyzed for each time step. The center-of-mass frame is chosen as the computational frame in our analysis. We have considered a cell of dimension $2 \times 2 \times 2$ fm^3 about the origin of Au + Au system. The test volume has been chosen such that the effect of collective flow of the system on the observables will be minimum and at the same time the particle number should be large enough for reasonably small fluctuation in the observables. Additionally a momentum rapidity cut $|y_{\rm c.m.}| < 1.0$ has been imposed on the particles under consideration to ensure that the beam nucleon contribution does not come into account. We have calculated the net particle density and different components of microscopic pressure for nonstrange baryons, strange baryons, and mesons inside the cell. The nonstrange baryons include proton (p) and neutron (n), the strange baryons include Λ, Σ, cascade (Ξ), and Ω, and the strange mesons include kaons K^+ and K^0. All the higher mass resonances (baryon and meson) are allowed to decay. We did not include Ω in the pressure calculation at $E_{\rm lab} = 10A$ and 20A GeV due to its limited statistics at lower energies. However, we expect that inclusion of Ω does not modify any conclusion drawn in this work. We have also calculated the energy spectra (EdN/d^3p vs E) of protons and Λs inside the cell. Lastly, the above quantities are statistically averaged over the number of events for each time step.

III. RESULTS

A. Time evolution of net particle density

The time (t) is the elapsed time in the center-of-mass frame. Time $t = 0$ fm/c corresponds to the moment when two nuclei touch each other. The net particle density $\rho(t)$ is defined as the difference of particle density and antiparticle density. The evolution of net nonstrange baryon density (ρ_B^{NS}), net strange baryon density (ρ_B^S), net kaon density (ρ_M^S), and net strange baryon to kaon ratio ($\rho_B^S/\ \rho_M^S$) are depicted in Fig. 1 at $E_{\rm lab} = 10A$, 20A, 30A, and 40A GeV. The net particle density starts from a small value, reaches a maximum around $t = 2R/(\gamma_{\rm c.m.} v_{\rm c.m.})$ when the two nuclei pass through each other, and then falls as the system expands. The generic feature has been found in agreement with earlier works [17,18]. Here R is the radius of Au nucleus and $\gamma_{\rm c.m.}$ and $v_{\rm c.m.}$ are the Lorentz boost and velocity in the center-of-mass frame. Thus we found the maximum matter densities near 6 fm/c at 10A GeV and 3 fm/c at 40A GeV for all species. The production of nonstrange baryons has been found to be similar for all beam energies, but the strange baryon and meson production becomes larger with increasing beam energy. This is probably because the string excitation mechanism has major contributions to strangeness production at higher energies. The peak of baryonic (nonstrange and strange) matter density has been found at 40A GeV, which is about 7–8 times the ground-state nuclear matter density. The time evolution of strange baryon to meson ratio has clearly shown the net strangeness content of the created matter is dominated by baryons for all the beam energies. The ratio has been found to grow with time because the kaons and Λs are produced through the same strong interaction. However, the kaons have suffered fewer scatterings in the medium due to its small interaction cross section with other hadrons [19], thus escaping the reaction volume quickly. The production of kaons is larger at higher beam energies, which can be seen from the nonmonotonus behavior of the ratio at smaller times.

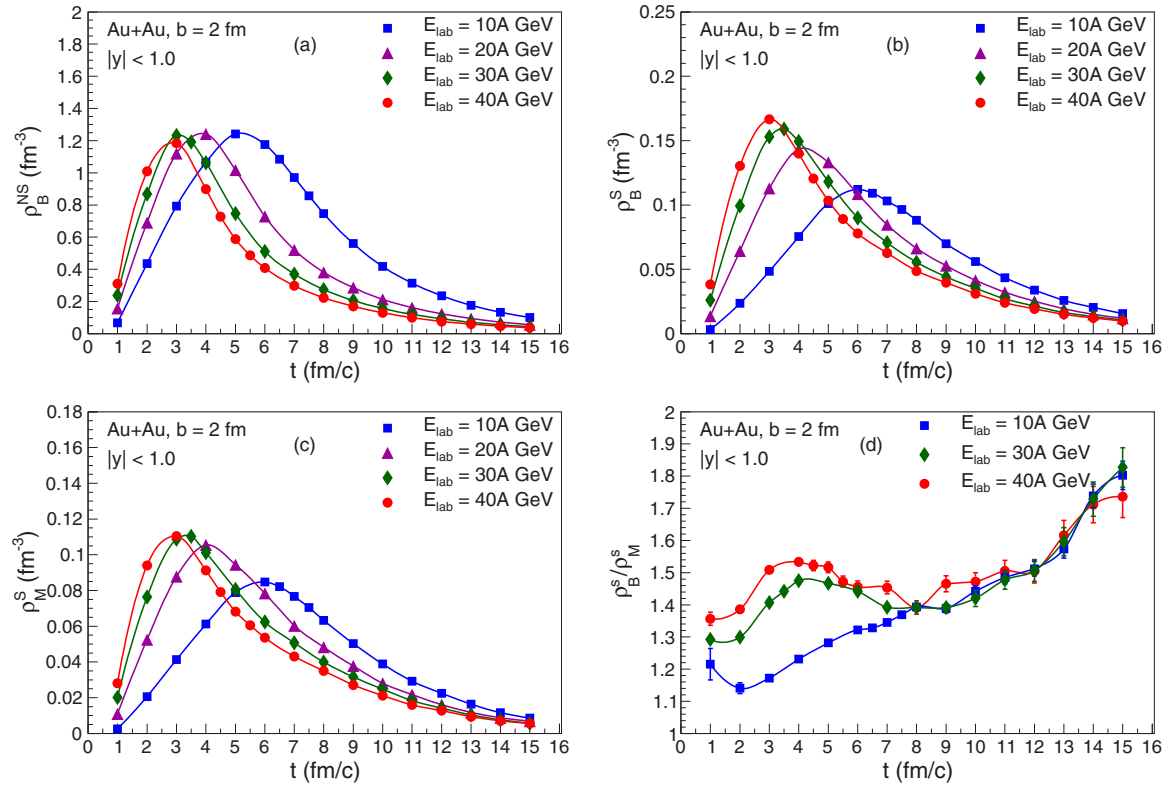

FIG. 1. (Upper panel) Time evolution of net density of (a) nonstrange baryons (ρ_B^{NS}), (b) strange baryons (ρ_B^S); (lower panel) (c) kaons (ρ_M^S) and (d) net strange baryon to kaon ratio ($\rho_B^S/\ \rho_M^S$) inside the central cell for Au + Au collisions ($b = 2$ fm) at the laboratory energies $10A$, $20A$, $30A$, and $40A$ GeV. The error bars are statistical only.

B. Isotropization of pressure components of baryons and mesons

We have studied the isotropization of different components of microscopic pressure of nonstrange baryons, strange baryons, and kaons for an expanding system. The pressure components are highly anisotropic immediately after the collision. Thermal equilibrium is established in the cell when the components have become nearly isotropic. Different components of microscopic pressure are calculated in UrQMD using the ideal gas ansatz [20]:

$$P_{(x,y,z)} = \sum_i \frac{p_{i(x,y,z)}^2}{3V\left(p_i^2 + m_i^2\right)^{\frac{1}{2}}}, \tag{1}$$

where p_i is the momentum, m_i is the mass of ith hadron, and V is the volume of the cell under consideration. The longitudinal and transverse components of pressure for an ensemble of hadrons are defined as

$$P_L = \langle P_z \rangle; \qquad P_T = \tfrac{1}{2}(\langle P_x \rangle + \langle P_y \rangle), \tag{2}$$

where $\langle\ \rangle$ corresponds to the statistical average over the number of events. The time evolution of the longitudinal-to-transverse pressure ratio (P_L/P_T) for the above-mentioned hadron species is shown in Fig. 2 at the four beam energies.

The P_L/P_T ratio of baryons (nonstrange and strange) starts from a large value at initial time and ultimately settles down to a value close to 1.0. This reflects the longitudinal (z) and transverse (x, y) momentum distribution of baryons, which are highly anisotropic at initial times. Successive elastic scatterings in the medium have made their momentum distribution nearly isotropic. We found that the ratio P_L/P_T becomes 1.0 around 6.5 fm for nonstrange baryons and 7 fm for strange baryons at $E_{\rm lab} = 10A$ GeV. However, the system further evolves and the ratio reaches a constant value ~ 0.8 for $t \geqslant 9$ fm/c. At this point we may say that the baryonic matter achieves a thermal equilibrium. Earlier work at AGS energy had also found similar time scale [20]. The deviation of P_L/P_T from unity after equilibrium possibly arises due to finite shear viscosity of the hadronic matter [21]. The ratio is closer to unity as the system approaches the ideal fluid limit. This has been shown by a recent study on the pressure isotropization in a quark-gluon plasma for Au + Au coliisions at top RHIC energy [22]. For other beam energies the P_L/P_T ratio of baryons has become unity much earlier, and it achieves a constant value ~ 0.8–0.7 for $t \geqslant 8$ fm/c at $20A$ GeV, for $t \geqslant 7$ fm/c at $30A$ GeV and for $t \geqslant 6$ fm/c at $40A$ GeV. On close inspection of Fig. 2, we found the pressure isotropization of nonstrange baryons happens a little earlier, $\Delta t \sim 0.5$ fm/c, than that for strange baryons. The observation is in concurrence with an earlier UrQMD-based calculation [23], which has shown the average freeze-out time of nucleons is smaller than the strange baryons (Λ, Ξ). The P_L/P_T ratio of kaons approaches to 1.0 at early times, $t \sim 3$ fm/c, and then becomes almost constant $\sim$0.6–0.7 at the same time as the baryons. The initial longitudinal-to-transverse

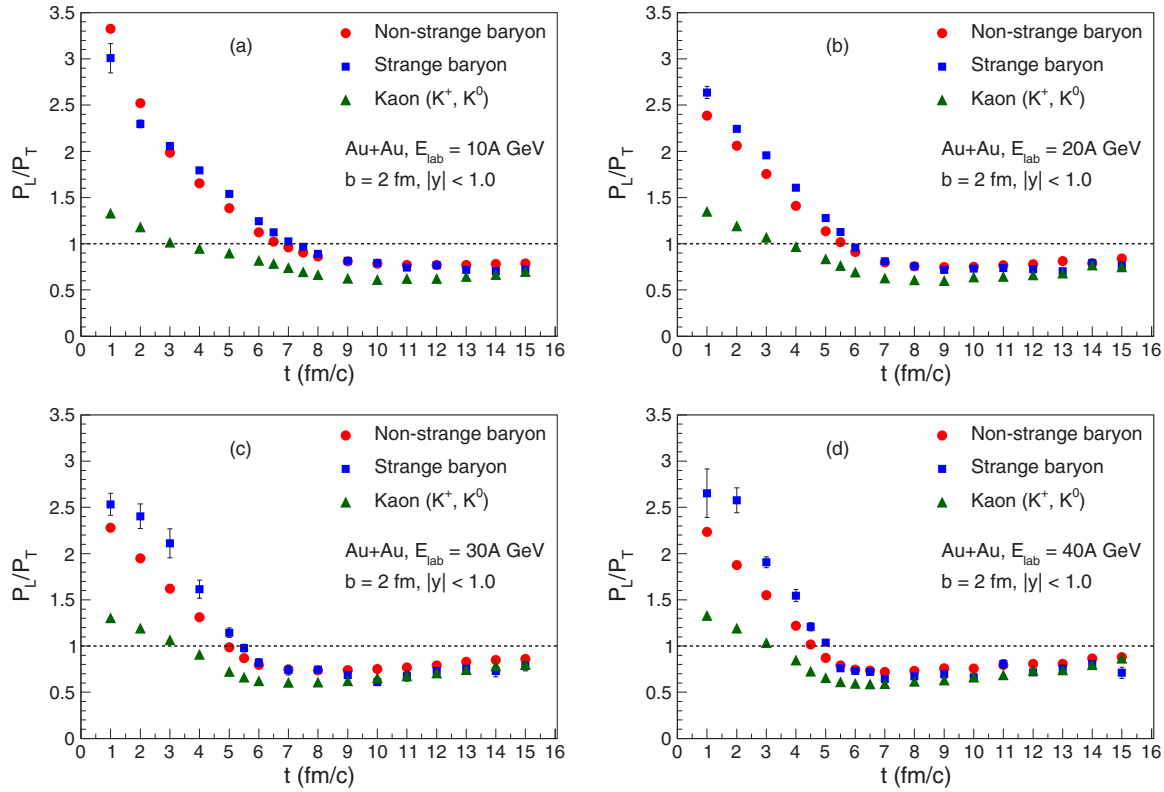

FIG. 2. Time evolution of longitudinal-to-transverse pressure ratio (P_L/P_T) of nonstrange baryons, strange baryons, and kaons inside the central cell for Au + Au collisions ($b = 2$ fm) at the laboratory energies (a) 10A, (b) 20A, (c) 30A, and (d) 40A GeV. The error bars are statistical only.

pressure (momentum) anisotropy of kaons has been found smaller than baryons, which could be because kaons have only one constituent quark from the original excited hadron and suffer fewer resonant scatterings than baryons in medium. Thus we found the pressure isotropization time of baryons and mesons reduces by about 3 fm/c from $E_{\rm lab} = 10A$ GeV to $E_{\rm lab} = 40A$ GeV.

C. Thermalization of energy spectra of baryons

In this section, we adopted an alternate approach to equilibrium which would reinforce the findings of earlier sections. We investigated the time scale of local thermalization of baryonic matter from the time evolution of inverse slope parameter of the energy spectra (EdN/d^3p vs E). For this purpose we have parameterized the energy spectra of proton and Λ inside the cell by Tsallis distribution [24]. An important criticism often arises is that systems obeying nonextensive statistics sometimes achieve thermal equilibrium or not. Here we refer to the work of Bíró and Purcsel [25], which has shown that two nonextensive subsystems do achieve a common equilibrium distribution within the framework of a nonextensive Boltzmann equation. The Tsallis distribution has extensively been used in recent years for describing the transverse momentum (p_T) distribution of produced hadrons at RHIC and the LHC energies [26,27]. The special merit of the distribution is that at a low-energy limit it reduces to an exponential distribution and at a high-energy limit it reduces to a power-law distribution [28]. Thus, it can accommodate both equilibrium and nonequilibrium phenomena. A recent work has found that the Tsallis distribution fits reasonably well for all particle spectra for $p_T < 10$ GeV at midrapidity in d + Au, Cu + Cu, and Au + Au collisions at RHIC [29]. Keeping these facts in mind, we write the energy spectra of proton and Λ inside the cell of dimension $2 \times 2 \times 2$ fm^3 about the origin of Au + Au system as

$$E\frac{d^3N}{d^3p} = C\left(1 + \frac{E}{bT}\right)^{-b}, \tag{3}$$

where E is the energy of baryon in the unit of GeV and $b = 1/(q-1)$ is dimensionless. C has the unit of Gev^{-2} and T is in GeV. q is called the nonextensive parameter of Tsallis distribution. The values of C, b, and T are obtained through fitting the energy spectra up to $E = 3$ GeV. The inverse slope parameter of this distribution is given by

$$T_{\rm slope} = T + (q-1)E. \tag{4}$$

In the asymptotic limit $E \to 0$, the inverse slope parameter ($T_{\rm slope}$) gives the thermodynamic temperature of the system [25]. We have calculated the $T_{\rm slope}$ of proton and Λ energy spectra at $E = 0.1$ GeV (nearly pion mass) and studied its time evolution at the four beam energies. The error in $T_{\rm slope}$ arises from the errors in the fitting parameters T and b. The results are depicted in Fig. 3.

We have found $T_{\rm slope}$ (for proton and Λ both) falls sharply with time and then almost scales as $\sim t^{-1/3}$ for $t \gtrsim 9$ fm/c at 10A GeV laboratory energy. If $T_{\rm slope}$ corresponds to the

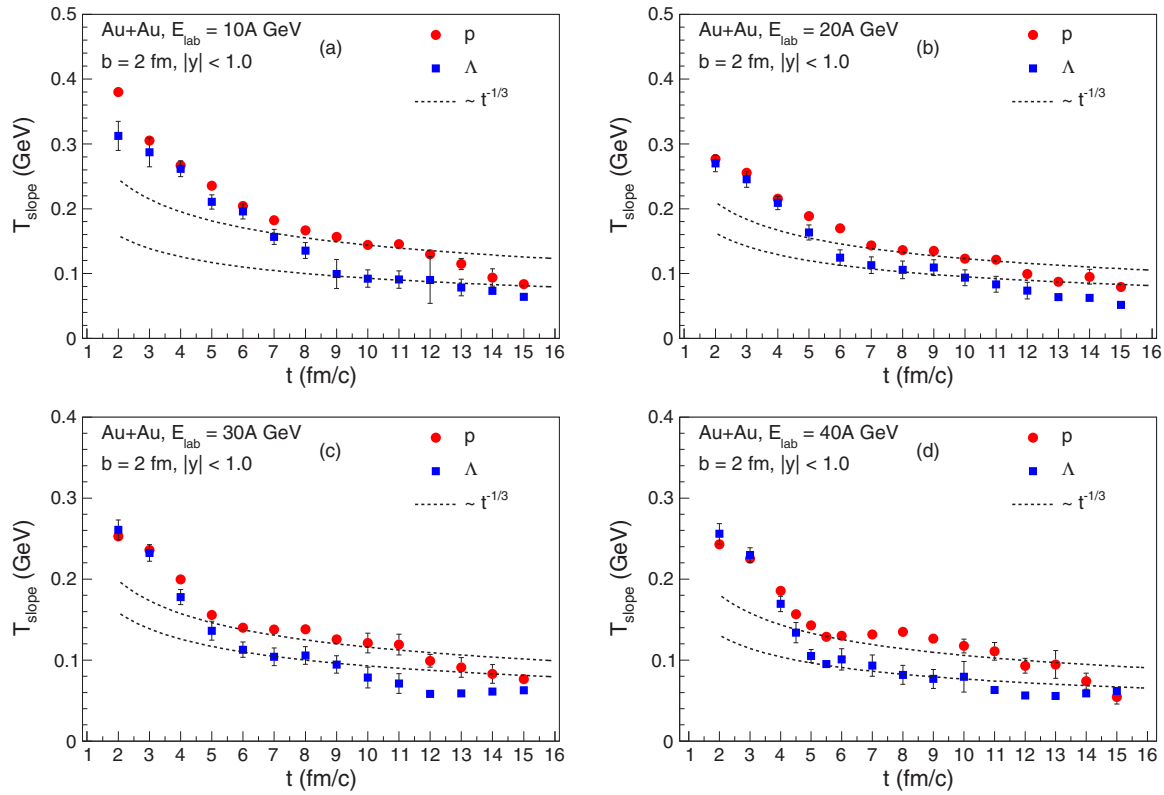

FIG. 3. Time evolution of the inverse slope parameter (T_{slope}) of the energy spectra of proton and Λ inside the central cell for Au+Au collisions ($b = 2$ fm) at the laboratory energies (a) 10A, (b) 20A, (c) 30A, and (d) 40A GeV. The error bars are statistical only.

local temperature of system, then we can infer an isentropic longitudinal expansion sets in inside the above-mentioned cell analogous to Bjorken ideal hydrodynamics. The temperature follows the Bjorken scaling solution. We consider the time as the local thermal equilibration time scale of the system at which the scaling behavior of the slope parameter has initiated. Similarly we have found the $t^{-1/3}$ scaling holds good for $t \gtrsim 7$ fm/c at 20A GeV, $t \gtrsim 6$ fm/c at 30A GeV, and $t \gtrsim 5$ fm/c at 40A GeV beam energy. At later times (say, $t > 10$ fm/c at $E_{\text{lab}} = 40A$ GeV), the T_{slope} is seen to scale as $\sim t^{-1}$ owing to the three-dimensional spherical expansion of the system (see Fig. 4). The assumption of the Bjorken hydrodynamic regime with the above-mentioned scaling solution, namely, initial one-dimensional flow and ideal gas equation of state, could be dubious at lower collision energies, although earlier works at AGS and SPS energies [30] have found phenomenological success based on it. However, it may be noted that we do not study thermalization of the whole reaction volume, but rather concentrate at the very central part of the system only. For this region, the above assumptions may be relevant; at least we can identify clearly the Bjorken scaling regime of T_{slope} for all energies (see Fig. 3). Thus we have found time

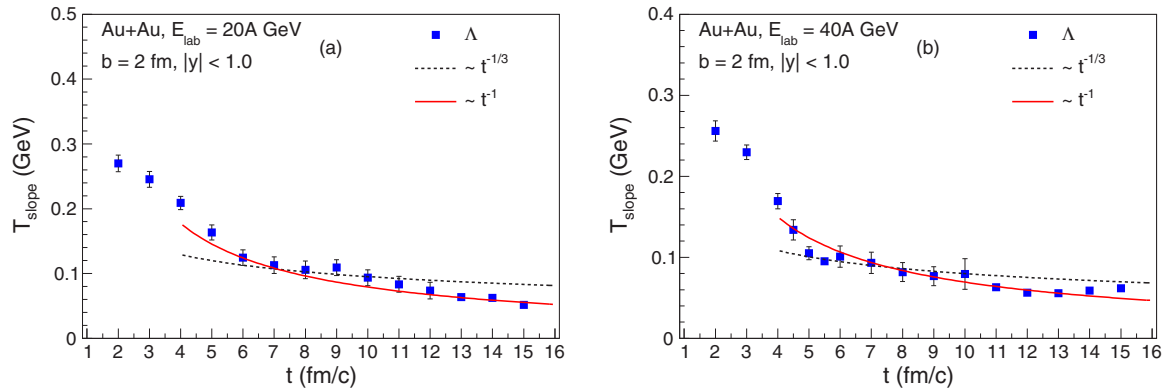

FIG. 4. The scaling behavior of inverse slope parameter (T_{slope}) of the energy spectra of Λ inside the central cell for Au+Au collisions ($b = 2$ fm) at (a) 20A and (b) 40A GeV laboratory energies. The black dotted line denotes the scaling due to longitudinal expansion and the red dashed line denotes scaling due to three-dimensional expansion. The error bars are statistical only.

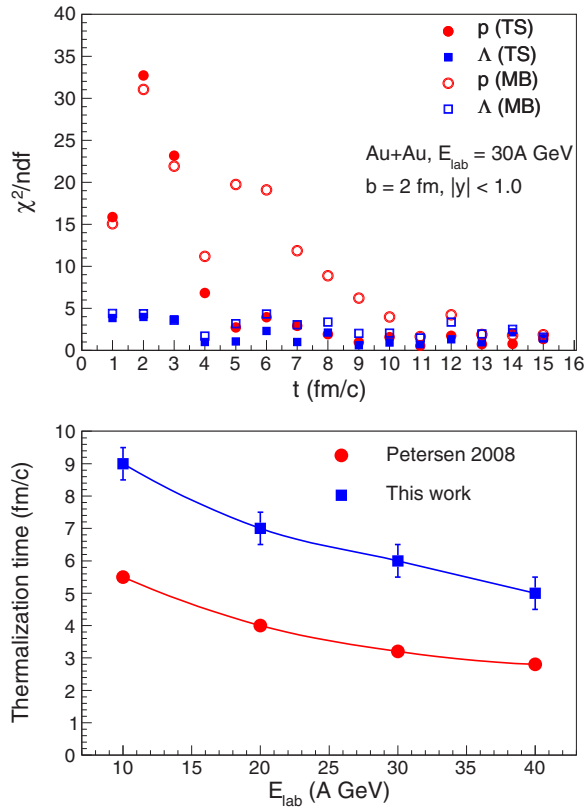

FIG. 5. (Upper panel) The χ^2 per degrees of freedom (χ^2/ndf) at different times for the Tsallis (filled symbols) and Maxwell-Boltzmann (open symbols) distribution which are fitted to the energy spectra of proton and Λ in the central cell for Au +Au collisions ($b = 2$ fm) at $E_{\rm lab} = 30A$ GeV. (Lower panel) The thermalization time obtained in this work (blue square) is compared with the local thermalization time $t_{\rm start}$ (red circle) used in the hybrid (UrQMD + hydrodynamics) model [31]. The error bars are considered to be systematic.

scale of thermalization of energy spectra roughly in agrees with the pressure isotropization time of baryons and decreases with the increase in laboratory energy for the above mentioned cell.

A natural question about the analysis involving $T_{\rm slope}$ is the following: How better does the Tsallis distribution fit the spectrum compared to any classical distribution? In order to see that, we fit the energy spectra of baryons with Maxwell-Boltzmann (MB) distribution: $f(E) = C'\exp[-(E-\mu)/T]$. C' is a constant, T is the temperature, and μ is the chemical potential in usual notation. We have fitted the spectra for Au +Au collisions at $E_{\rm lab} = 30A$ GeV for the same range of E and calculated the χ^2 per degrees of freedom (χ^2/ndf) for different times. The result is depicted in Fig. 5. It has been observed that the Tsallis distribution mostly gives a lower value of χ^2/ndf which is close to unity in comparison to the MB distribution. The inverse slope parameters of both distributions at different times are listed in Table I.

Several facts emerge upon close inspection. First, the two parameters are very similar at early times (say, up to 3 fm/c). This might be due to numerical equivalance of the two distributions at these times. However, it can be noted that χ^2/ndf comes out very large at those times for both distributions; thus the parameters may not be describing a good fit.

TABLE I. The inverse slope parameters for Tsallis and Maxwell-Boltzmann distributions at different times. The distributions are fitted to the energy spectra of protons in the central cell for Au+Au collisions at $E_{\rm lab} = 30A$ GeV.

t (fm/c)	$T_{\rm slope}$(Tsallis) (GeV)	T(MB) (GeV)
1	0.275	0.267
2	0.252	0.247
4	0.200	0.223
6	0.140	0.195
8	0.138	0.178
10	0.121	0.161
12	0.099	0.138
14	0.083	0.116

Now in the thermal regime, say for $t \geqslant 6$ fm/c, the two parameters differ by nearly 40 MeV and $T_{\rm slope}$ (Tsallis) is smaller than T(MB). The behavior has been studied in Ref. [32]. The Tsallis distribution describes a near-thermal equilibrium situation for q value close to unity. For the same particle yield, Tsallis distribution leads to lower temperature (i.e., inverse slope parameter) than MB distribution for $q > 1$. The Tsallis temperature often interpreted as the superposition of different MB temperatures and the relative width of fluctuation in T (MB) is related to the nonextensivity parameter $(q-1)$ [33]. We have checked that $(q-1)$ remains almost constant at $\sim$0.03 during the time span. The constant difference between the slope parameters can be attributed to this fact. A similar trend between the inverse slope parameters has been reported in Ref. [34] where the particle spectra for central Pb-Pb collisions at the LHC energy are fitted with both Tsallis and MB distribution.

D. A comparison with earlier work

We have compared our result with the local thermalization time scale ($t_{\rm start}$) used by an earlier work of hybrid model of Boltzmann transport and hydrodynamics by Petersen *et al.* [31]. The model has successfully described the data of rapidity-dependent yield and transverse mass spectra of hadrons at AGS and SPS experiments. The $t_{\rm start}$ is considered *ad hoc* as the nuclear passage time in the center-of-mass frame. The comparison can be found in Fig. 5. We have introduced a systematic uncertainty of ± 0.5 fm in our estimated thermalization time because the simulation was carried out in time steps of $\Delta t = 1$ fm. It has been found that our result decreases with increasing laboratory energy similar to $t_{\rm start}$ but is about 1.5 times larger in magnitude. The earlier work has assumed that $t_{\rm start}$ is the lowest possible time needed for local thermalization; however, the current study could provide a more realistic estimate of it. Nevertheless, the issue has been investigated further in Ref. [31], which found that multiplicity and mean transverse momenta of particles do not change appreciably when $t_{\rm start}$ increases by factor of 2.

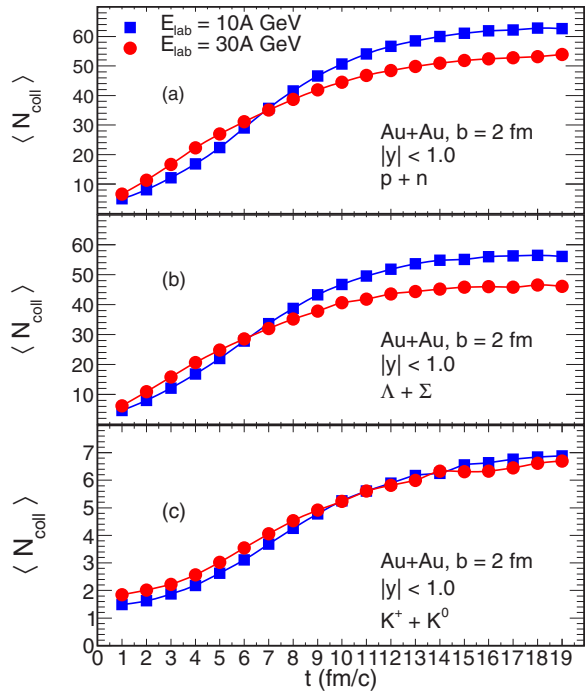

FIG. 6. Time evolution of average number of collisions ($\langle N_{\rm coll}(t)\rangle$) suffered by (a) protons and neutrons, (b) Λ and Σ baryons, and (c) kaons for Au + Au collisions ($b = 2$ fm) at laboratory energies 10A and 30A GeV.

IV. COMPARISON WITH STATISTICAL THERMAL MODEL

In the preceding sections we argued that the dense hadronic matter created in the collisions will achieve local thermal equilibrium on a certain time scale. Thus we can employ the statistical hadron gas model [35] to extract the intensive thermodynamic variables like temperature and chemical potential of the system during subsequent evolution. The statistical model cannot be applied prior to equilibrium but can be applied beyond thermal freeze-out of the system. Traditionally thermal freeze-out is defined as the average scattering rate between the constituents becomes smaller than the average expansion rate of the system. The system has become so dilute that hardly any collision between the constituents takes place. Following this criterion, we have checked the time evolution of the average number of collisions ($\langle N_{\rm coll}(t)\rangle$) suffered by different hadron species. Figure 6 shows that average number of collisions suffered by p, n, Λ, Σ baryons, and K mesons almost saturate for $t \gtrsim 17$ fm/c at $E_{\rm lab} = 10A$ GeV and $t \gtrsim 15$ fm/c at $E_{\rm lab} = 30A$ GeV. Considering the above scenarios, we compared the statistical model with UrQMD during the time interval 10 fm/c $\leqslant t \leqslant$ 17 fm/c at 10A GeV and 8 fm/c $\leqslant t \leqslant$ 15 fm/c at 30A GeV laboratory energy.

The expressions for number density and energy density for the ith hadron species in the statistical hadron gas model are given by

$$n_i = \frac{g_i}{(2\pi\hbar)^3}\int 4\pi p^2 f_i(T,\mu_i)\,dp,$$

$$\varepsilon_i = \frac{g_i}{(2\pi\hbar)^3}\int 4\pi p^2 e_i\, f_i(T,\mu_i)\,dp,$$

TABLE II. The time evolution of temperature (T), baryon chemical potential (μ_B), and strange chemical potential (μ_s) in the central cell ($2\times2\times2$ fm^3) for Au + Au collisions ($b = 2$ fm) at laboratory energies of 10A and 30A GeV. The thermodynamic parameters are obtained from the energy density of baryons (ε_B), number density of baryons (n_B), and number density of strange hadrons (n_s) using a statistical hadron gas model.

$E_{\rm lab} = 10A$ GeV				$E_{\rm lab} = 30A$ GeV			
t (fm/c)	T (GeV)	μ_B (GeV)	μ_s (GeV)	t (fm/c)	T (GeV)	μ_B (GeV)	μ_s (GeV)
10	0.145	0.708	0.174	8	0.152	0.616	0.123
11	0.136	0.697	0.148	9	0.145	0.601	0.100
12	0.128	0.687	0.125	10	0.137	0.595	0.081
13	0.120	0.680	0.102	11	0.129	0.593	0.067
14	0.114	0.670	0.082	12	0.123	0.587	0.047
15	0.108	0.664	0.070	13	0.115	0.586	0.031
16	0.102	0.659	0.049	14	0.110	0.586	0.019
17	0.097	0.656	0.041	15	0.105	0.585	0.011

where e_i is the energy, T is the temperature, and μ_i is chemical potential of the ith hadron. The hadrons are considered relativistic, $e_i = (p^2 + m_i^2)^{\frac{1}{2}}$. f_i is the distribution function of the ith hadron (either Fermi-Dirac or Bose-Einstein). However, the above distributions are practically approximated to classical MB distribution as $(e_i - \mu_i)/T \gg 1$. μ_i can be decomposed in terms of baryonic (μ_B) and strange (μ_s) chemical potentials. The charge chemical potential (μ_Q), which is an order of magnitude smaller than the other two, has been neglected here:

$$\mu_i = b_i\mu_B + s_i\mu_s,$$

where b and s are the baryon and strangeness quantum number respectively. T, μ_B, and μ_s are extracted from the following equations:

$$\varepsilon_B = \sum_i^{\rm baryon}\varepsilon_i,\ n_B = \sum_i^{\rm baryon} b_i n_i,\ n_s = \sum_i^{\rm baryon,meson} s_i n_i. \quad (5)$$

The quantities in the left-hand side of Eq. (5), namely energy density of baryons (ε_B), number density of baryons (n_B), and number density of strange hadrons (n_s), are obtained from the UrQMD. We have solved the above set of equations during the time interval stated earlier. The values are listed in Table II. We have plotted them in the QCD phase diagram in order to get an estimate about the chemical and thermal freeze-out time of the system (see Fig. 7). The chemical freeze-out line has been obtained empirically from the thermal model fit of particle ratios at different collision energies [36]. The thermal or kinetic freeze-out line has also been obtained phenomenologically from the blast wave model fits of the measured hadron spectra at different experiments [37]. It can be seen at low energies $E_{\rm lab} = 10A$ GeV, the chemical and the kinetic freeze-out happens almost instantaneously at $t \approx 17$ fm/c. At higher energy $E_{\rm lab} = 30A$ GeV, system undergoes first chemical freeze-out at $t \approx 13$ fm/c, and then kinetic freeze-out at $t \approx 15$ fm/c. The feature has already

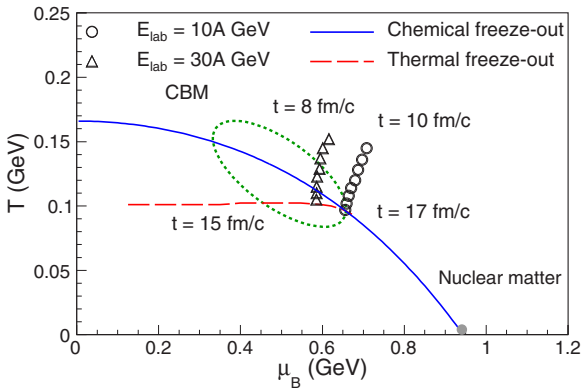

FIG. 7. The evolution of temperature (T) and baryochemical potential (μ_B) in the central cell for Au + Au collisions ($b = 2$ fm) at $E_{\rm lab} = 10A$ GeV and $30A$ GeV. The solid (blue) line denotes the chemical freeze-out and the dashed (red) line denotes thermal freeze-out boundary in relativistic heavy ion collisions [36,37]. The dotted circle denotes the expected region probed by the CBM experiment ($\sqrt{s_{NN}} = 4$–10 GeV) at FAIR.

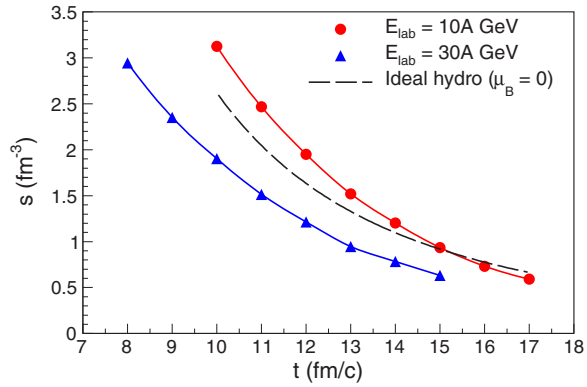

FIG. 8. The time evolution of entropy density of baryonic matter inside the central cell for Au +Au collisions (b = 2 fm) at $E_{\rm lab} = 10A$ GeV and $30A$ GeV. The dashed line denotes the parametrization of ideal hydrodynamic evolution of entropy density in the central region for Au +Au collisions (b = 0 fm) at $\sqrt{s_{NN}} = 200$ GeV [44].

observed in low-energy collision experiments at RHIC [38]. We would also like to add that our estimation of temperatures at the kinetic freeze-out times closely agree with the values given by the blast wave model fit to the Λ baryon spectra from the NA49 Collaboration at the similar laboratory energies [15].

We are interested in computing bulk properties of a baryon-rich hadronic medium, and thus the strange meson contribution can be neglected as $\mu_s \rho_M^S \approx$ few MeV. Using the values of temperature and chemical potential listed in Table II, we have calculated the pressure of baryons with the statistical hadron gas model:

$$P = \sum_{i}^{baryon} \frac{g_i}{(2\pi\hbar)^3} \int 4\pi p^2 dp \frac{p^2}{3\left(p^2 + m_i^2\right)^{\frac{1}{2}}} f_i(T, \mu_i), \quad (6)$$

and the entropy density (s) for baryons using the thermodynamic relation:

$$Ts = \varepsilon_B + P - \mu_i\left(\rho_B^{NS} + \rho_B^S\right), \quad (7)$$

where μ_i is the chemical potential, defined earlier in this section. We studied the time evolution of entropy density at $E_{\rm lab} = 10A$ and $30A$ GeV until thermal decoupling. Our aim is to get some insight about the fluidity of the dense baryonic matter created in these collisions. In recent times several calculations [39–41] have been reported on the transport properties of hadronic matter at finite baryochemical potential, including the effect of high mass resonances, etc. However, the fluidity of dense hadronic matter was discussed in Ref. [40] and subsequently in Refs. [42,43]. The authors of Ref. [40] have argued that the fluid behavior of a baryon-rich ($\mu_B \sim$ 500 MeV) hadron gas is closer to the ideal fluid limit than the corresponding gas with zero baryon number. Following their observation, we have compared the entropy densities at $E_{\rm lab} = 10A$ and $30A$ GeV with the ideal fluid limit reached at the highest RHIC energy ($\sqrt{s_{NN}} = 200$ GeV). We have parameterized temporal evolution of entropy density of hadronic matter from an ideal hydrodynamic simulation [44] for central Au +Au collisions at $\sqrt{s_{NN}} = 200$ GeV. The entropy density at $r = 3$ fm from the center has been found to scale with proper time (τ) as $\sim \tau^{-2.6}$ for $\tau \geqslant 10$ fm/c. The results are depicted in Fig. 8 along with the parameterization from ideal hydrodynamics. It is heartening to see that the evolution of entropy density at $E_{\rm lab} = 30A$ GeV closely resembles that with ideal hydrodynamic limit at zero net baryon density. The entropy density at $E_{\rm lab} = 10A$ GeV falls even a little faster than the aforementioned limit. It may imply that the hadronic matter produced at $10A$ GeV beam energy is more ideal than the same at $30A$ GeV beam energy. The observation can be understood using the fact that shear viscosity to entropy density ratio (η/s) of a hadronic system decreases with increasing fugacity (μ_B/T) of the system [21].

V. SUMMARY AND DISCUSSION

In this article, we have investigated the time scale for local thermal equilibration of dense baryonic matter created in central Au + Au collisions at the proposed CBM experiment energies of $E_{\rm lab} = 10A$, $20A$, $30A$, and $40A$ GeV. The microscopic transport model UrQMD has been used for this purpose in the default cascade mode. The net baryon density has been found maximum at 30–40 GeV and the net strangeness of the created hadronic matter is dominated by baryons for all energies stated above. We have studied the time evolution of longitudinal-to-transverse microscopic pressure anisotropy and inverse slope parameter of the energy spectra of baryons and mesons inside a cell of 8 fm^3 in the central region of Au + Au system. The pressure anisotropy ratio of baryons and mesons has achieved a constant value close to unity, at a certain time. The time has been found to decrease with the increase in laboratory energy. The time scale obtained from the evolution of inverse slope parameter of energy spectra of baryons nearly agrees with the pressure (or momentum) isotropization time. However, a small time difference ($\Delta t \sim 0.5$ fm/c) in the pressure isotropization as well as in the thermalization of energy spectra between strange and nonstrange baryons has been noticed. We have chosen

our test volume in the central collision zone. The estimated time scales are expected to grow in a region which is away from the center because of small scattering rates. Therefore, the present study provides a realistic estimate of the time scales required for achieving thermodynamic equilibrium for the central region of the system created at those energies.

Using a statistical thermal model, we have obtained the temperature and chemical potentials of the hadronic matter during the post-equilibrium evolution at $E_{\rm lab} = 10A$ and $30A$ GeV. They are found to agree qualitatively with the empirical relation between T and μ_B at the chemical freeze-out. In addition we have calculated the entropy density of the baryonic matter inside the cell and found the evolution is quasi-isentropic, close to the ideal hydrodynamic limit at zero net baryon density.

ACKNOWLEDGMENTS

The work is partially supported by Bose Institute Indo-Fair Coordination Centre (BI-IFCC). We are thankful to Grid tier-2 center, Kolkata, for providing computing resources. We acknowledge the financial assistance from Department of Atomic Energy (DAE), India, and Fundação de Amparo à Pesquisa do Estado de Sã Paulo (FAPESP), Brazil, during the course of the work.

[1] B. B. Back *et al.*, Nucl. Phys. A **757**, 28 (2005).
[2] N. Armesto *et al.*, J. Phys. G **35**, 054001 (2008).
[3] O. Philipsen, Prog. Part. Nucl. Phys. **70**, 55 (2013).
[4] N. Xu (STAR Collaboration), Nucl. Phys. A **931**, 1 (2014).
[5] S. Chattopadhyay, J. Phys. G **35**, 104027 (2008).
[6] B. Friman *et al.*, *The CBM Physics Book*, Lecture Notes in Physics Vol. 814 (Springer-Verlag, Berlin, 2010).
[7] P. Senger, Prog. Part. Nucl. Phys. **62**, 375 (2009).
[8] V. I. Kolesnikov and A. I. Zinchenko, arXiv:1312.1091 [nucl-ex].
[9] H. R. Schmidt (CBM Collaboration), PoS (Bormio 2013) 061.
[10] R. Baier, A. H. Mueller, D. Schiff, and D. T. Son, Phys. Lett. B **502**, 51 (2001).
[11] F. Gelis, Nucl. Phys. A **931**, 73 (2014).
[12] S. A. Bass *et al.*, Prog. Part. Nucl. Phys. **41**, 225 (1998); M. Bleicher *et al.*, J. Phys. G **25**, 1859 (1999).
[13] W. Cassing, E. L. Bratkovskaya, and S. Juchem, Nucl. Phys. A **674**, 249 (2000).
[14] Z. W. Lin, C. M. Ko, B. A. Li, B. Zhang, and S. Pal, Phys. Rev. C **72**, 064901 (2005).
[15] C. Alt *et al.* (NA49 Collaboration), Phys. Rev. C **78**, 034918 (2008).
[16] J. Cugnon, Phys. Rev. C **22**, 1885 (1980).
[17] I. C. Arsene, L. V. Bravina, W. Cassing, Y. B. Ivanov, A. Larionov, J. Randrup, V. N. Russkikh, V. D. Toneev, G. Zeeb, and D. Zschiesche, Phys. Rev. C **75**, 034902 (2007).
[18] B. Friman, W. Norenberg, and V. D. Toneev, Eur. Phys. J. A **3**, 165 (1998).
[19] G. Q. Li, C. H. Lee, and G. E. Brown, Nucl. Phys. A **625**, 372 (1997).
[20] L. V. Bravina *et al.*, Phys. Lett. B **434**, 379 (1998).
[21] N. Demir and S. A. Bass, Phys. Rev. Lett. **102**, 172302 (2009).
[22] M. Ruggieri, F. Scardina, S. Plumari, and V. Greco, Phys. Rev. C **89**, 054914 (2014).
[23] Z. Xie, P. Ning, and S. A. Bass, J. Phys. G **37**, 045002 (2010).
[24] C. Tsallis, J. Stat. Phys. **52**, 479 (1988).
[25] T. S. Bíró and G. Purcsel, Phys. Lett. A **372**, 1174 (2008).
[26] J. Cleymans and D. Worku, Eur. Phys. J. A **48**, 160 (2012).
[27] P. K. Khandai, P. Sett, P. Shukla, and V. Singh, J. Phys. G **41**, 025105 (2014).
[28] C. Y. Wong and G. Wilk, Acta Phys. Pol. B **43**, 2047 (2012).
[29] H. Zheng and L. Zhu, Adv. High Energy Phys. **2015**, 180491 (2015).
[30] P. F. Kolb, J. Solfrank, and U. Heinz, Phys. Lett. B **459**, 667 (1999); H. Dobler, J. Solfrank, and U. Heinz, *ibid.* **457**, 353 (1999).
[31] H. Petersen, J. Steinheimer, G. Burau, M. Bleicher, and H. Stöcker, Phys. Rev. C **78**, 044901 (2008).
[32] J. Cleymans, G. Hamar, P. Levai, and S. Wheaton, J. Phys. G **36**, 064018 (2009).
[33] G. Wilk and Z. Wlodarczyk, Phys. Rev. Lett. **84**, 2770 (2000).
[34] F. H. Liu, Y. Q. Gao, and B. C. Li, Eur. Phys. J. A **50**, 123 (2014).
[35] P. Braun-Munzinger, K. Redlich, and J. Stachel, arXiv:nucl-th/0304013 (unpublished).
[36] J. Cleymans, H. Oeschler, K. Redlich, and S. Wheaton, Phys. Rev. C **73**, 034905 (2006).
[37] U. W. Heinz, *Relativistic Heavy Ion Physics*, Landolt-Boernstein New Series, Vol. I/23, edited by R. Stock (Springer Verlag, New York, 2010), Chap. 5, and references therein.
[38] B. Mohanty, Nucl. Phys. A **830**, 899C (2009).
[39] K. Itakura, O. Morimatsu, and H. Otomo, Phys. Rev. D **77**, 014014 (2008).
[40] G. S. Denicol, C. Gale, S. Jeon, and J. Noronha, Phys. Rev. C **88**, 064901 (2013).
[41] G. P. Kadam and H. Mishra, Nucl. Phys. A **934**, 133 (2014).
[42] S. Ghosh, Phys. Rev. C **90**, 025202 (2014).
[43] G. P. Kadam and H. Mishra, Phys. Rev. C **92**, 035203 (2015).
[44] P. F. Kolb and U. Heinz, arXiv:nucl-th/0305084 (unpublished).